The local atomic structure and thermoelectric properties of Ir-doped ZnO: hybrid DFT calculations and XAS experiments

Andrei Chesnokov[a], Denis Gryaznov*[a], Natalia V. Skorodumova[b,c] , Eugene A. Kotomin[a,d] , Andrea Zitolo[e], Martins Zubkins[a] , Alexei Kuzmin[a], Andris Anspoks[a] and Juris Purans[a]

We combined the hybrid density functional theory (DFT) calculations and X-ray absorption spectroscopy (XAS) experiments in the study of the local atomic structure around Ir ions in ZnO thin films with different iridium content. This is then used in the first principles analysis of thermoelectric properties of material. The emphasis has been put on the conditions for a positive Seebeck coefficient and p-type electrical conductivity as the functions of Fermi level. We studied both computationally and experimentally several possible IrO_x polyhedra (complexes) with different number of surrounding oxygens and Ir oxidation states, including those with the formation of peroxide ion (O_2^{2-}). In particular, octahedral coordination of iridium ions was identified by reverse Monte Carlo (RMC) simulations of the Ir L_3-edge EXAFS spectra of ZnO:Ir thin films as the predominant complex, which is supported by the calculated lowest interstitial oxygens incorporation energies. All the calculated IrO_x (x = 4,5,6) complexes, regardless of Ir oxidation state, demonstrate a potential for the p-type conduction if the Fermi level (μ_F) falls into the range 0-0.8 eV from the valence band maximum (VBM) and the Ir concentration is high enough (12.5% in the present DFT calculations). Even though the corresponding calculated Seebeck coefficient (S) around 80-89 μVK^{-1} slightly exceeds the experimental values, we emphasise the presence of important plateau in the dependence of S on μ_F in this range for two complexes with the formation of peroxide ions (O_2^{2-}). We predicted also that peroxide ions O_2^{2-} are characterized by the calculated phonon frequencies of 810-942 cm^{-1} in agreement with our previous Raman experimental results. In this light, we discuss the high sensitivity of calculated $S(\mu_F)$ dependences to the atomic and electronic structure.

Introduction

Zinc oxide (ZnO) is widely used in semiconductor and optoelectronic industries. Despite more than two decades of intensive research, the capabilities of ZnO are still not exhausted. It can be grown as large bulk single crystals of high quality, deposited as thin films, or made amorphous[1–3]. It has a 3.4 eV wide band gap, strong luminescence, high electron mobility, high thermal conductivity and large exciton binding energy. Due to these properties, ZnO is regarded as a promising material for a wide variety of applications, including but not limited to transparent conductors, sensors/emitters of blue and UV light, and to functional coatings[4,5]. In particular, modern electronics requires stable p-type thin films with sufficiently high transparency and p-type conductivity. Modified ZnO can be a stable n-type conductor, and the current research focuses on achieving stable p-type conductivity. Concurrently, as a result of advances in growing methods, research scope is also shifting towards an amorphous phase of ZnO[6].

To the date, there is a room for more details on a study of behaviour of intrinsic and impurity defects in ZnO. A comprehensive analysis of intrinsic defects' behaviour by using advanced optical measurements was recently performed for defect-rich single ZnO[7] crystals. In the interpretation of photo-luminescence spectra the oxygen vacancies (V_O), the vacancies pairs (V_O-V_{Zn}), Zn interstitials and their complexes were identified. In ZnO electronic donors are formed spontaneously leading to intrinsic doping asymmetry[8]. Even though the oxygen vacancy possesses the lowest formation energy under Zn and O-rich conditions in most theoretical studies on bulk material, understanding conditions for the growth of the thin films plays a very important role. The literature indicates that the analysis of defects in thin films should be done with caution. For instance, the Mn-doped ZnO thin films required theoretical computations to explain discrepancies in the interpretation of XANES (X-ray absorption near edge structure)

a. Institute of Solid State Physics, University of Latvia, Kengaraga 8, Riga, LV-1063, Latvia.
b. Department of Materials Science and Engineering, School of Industrial Engineering and Management, KTH-Royal Institute of Technology, Brinellvägen 23, Stockholm, Sweden.
c. Department of Physics and Astronomy, Uppsala University, Box 516, 751 20 Uppsala, Sweden.
d. Max Planck Institute for Solid State Research, Heisenbergstr. 1, Stuttgart, D-70569, Germany.
e. Synchrotron SOLEIL, L'orme des Merisiers, BP 48 Saint Aubin, 91192, Gif-sur-Yvette, France.
† Footnotes relating to the title and/or authors should appear here.
Electronic Supplementary Information (ESI) available: [details of any supplementary information available should be included here]. See DOI: 10.1039/x0xx00000x

spectra[9]. It was established that neither O nor Zn vacancy are detectable in the XANES spectra. Their presence is less important than local structure changes induced by the Mn impurity. The present study focuses on the d-electron impurity, Ir. ZnO:cIr thin films (c is the Ir concentration) have demonstrated the change in the sign of Seebeck coefficient from a negative to positive for Ir concentration ranging from c=12.4 to 16.4%[10]. High oxygen partial pressure during the ZnO:cIr thin films deposition and films' transformation into amorphous phase with the Ir concentration c=7-16% at room temperature allows to suggest an important role of oxygen interstitials (O_i's)[10]. However, atomistic understanding of the ZnO:cIr thin films' properties changes was missing. Notice that the present experiments considered a wider range of Ir concentrations and were mainly focused on the local atomic structure around Ir. The Raman spectroscopy revealed[10] the existence of a vibrational band at 720 cm^{-1}, and it was argued that its presence is not due to IrO$_2$ phase but is rather related to the formation of peroxide moiety (O_2^{2-}). The existing body of work[5] related to ZnO largely agrees on the fact that O_i tend to form an O-O 'dumbbell' or 'split interstitial'. It may show both donor- and acceptor-like qualities as discussed based on DFT calculations[11].

Notice that previous DFT calculations of Ir-doped ZnO did not discuss the thermoelectric properties and the effect of Seebeck coefficient sign change[12–14]. Thus, the present DFT calculations address these peculiar properties of ZnO:Ir thin films and explore the connection between the role of Ir impurity and O_i for the electronic structure, thermoelectrical properties and p-type conduction. We use several models of IrO$_x$ polyhedra (called, hereafter, IrO$_x$ complexes) in ZnO, distinguished by the number of oxygens surrounding Ir, the oxidation state of Ir, incorporation energy of O_i's and a presence of peroxide defects. Thus, we can find interpretations in the Seebeck coefficient dependences on μ$_F$ for potential p-type conduction in Ir-doped ZnO.

Experimental section describes details of preparing Ir-doped ZnO and pure IrO$_x$ thin films and synchrotron radiation XAS measurements at the Ir L$_3$-edge. Subsequent sections on methods introduce the models for the calculation of IrO$_x$ complexes in ZnO and presents computational details, including those regarding the thermoelectric properties. Results' section is divided into several subsections to discuss the results of the extended X-ray absorption fine structure (EXAFS) spectra analysis using reverse Monte Carlo (RMC) simulations, the calculated structural properties of IrO$_x$ complexes in ZnO and those of the parent compounds, the electronic structure properties of IrO$_x$ complexes in ZnO, and the main results of thermoelectric properties calculations.

Methods

Experimental

Mixed zinc-iridium oxide (ZnO:cIr) and pure IrO$_x$ amorphous thin films were deposited on polyimide tape substrates at room temperature by reactive DC magnetron co-sputtering in an Ar (20 sccm) + O$_2$ (10 sccm) atmosphere (10 mTorr working pressure). A metallic Zn (99.95 wt%) target with Ir (99.6 wt%) pieces placed on the target erosion zone were used for sputtering. The thin film thickness was about 200-300 nm. The iridium concentration (c=7%, 16%, 29%, 54% and 67%) was determined using X-ray fluorescence measurements. X-ray diffraction measurements confirm the amorphous structure of all films. More details about the experimental procedure can be found in Ref. 10.

X-ray absorption spectra (XAS) at the Ir L$_3$-edge were measured at room temperature at SAMBA bending-magnet beamline[15] of the Synchrotron SOLEIL storage ring. The experiments were performed in transmission mode using the focusing Si(220) monochromator and two ionization chambers. For each sample, a multi-layered sandwich was prepared to obtain a sufficiently large total thickness of samples with an absorption edge jump close to 1. The processing of XAS was performed using a conventional procedure[9], as implemented in the XAESA code[16].

The Ir L$_3$-edge EXAFS spectra in mixed zinc-iridium oxide (ZnO:cIr) and pure IrO$_x$ thin films were analysed using the reverse Monte Carlo (RMC) method[17] based on the evolutionary algorithm (EA), which is implemented in the EvAX code[18].

DFT calculations

We have performed all DFT calculations using the CRYSTAL17 v 1.0.2 [19–22] computer code. We used the supercell approach[23], and as such we have modelled defective structures of ZnO (wurtzite structure with four atoms per unit cell, space group $P6_3mc$) using 2×2×1 (i.e. four times extended unit cell L4, consisting of 16 atoms) or 4×4×3 (L48, 192 atoms) supercells. These supercells represented 12.5 (L4) and 1.04 (L48) atomic % concentrations of Ir. In all cases, Ir ion substituted a regular Zn ion. In the following analysis, we refer to this defect as $Ir^{n+}O_x$ complex, where n denotes the oxidation state[24] and x is the number of oxygen ions adjacent to Ir. In wurtzite structure, Zn has four nearest O ions. Thus, we first model Ir surrounded by four host oxygen ions. In results section we will show that n = 2 in this case, i.e. $Ir^{2+}O_4$. Other complexes included the O_i ions. In our calculations we considered numerous atomic configurations and used the incorporation energy of O_i's (discussed below) to choose the most important ones. There is a different complex with four oxygen ions surrounding Ir but with n = 3, i.e. $Ir^{3+}O_4$, due to only one O_i adjacent to Ir and simultaneously forming O_2^{2-} with a host oxygen (our first complex with the formation of O_2^{2-}). There is the complex with five oxygen ions surrounding Ir with n = 4, i.e. $Ir^{4+}O_5$, due to two O_i's close to Ir. In this complex one of the O_i ions forms O_2^{2-} with the host oxygen (our second complex with the formation of O_2^{2-}). Lastly, there is the complex with six oxygen ions surrounding Ir with n = 4, i.e. $Ir^{4+}O_6$, due to two O_i's close to Ir and without formation of O_2^{2-}. The atomic structure of each complex after the full structure relaxation can be seen in fig. 5 and in fig. S1.

We analyse the oxidation state n of $Ir^{n+}O_x$ in the different complexes by comparing it to reference materials: IrO_2 (formal oxidation state of iridium is 4+), a hypothetical Ir_2O_3 (formal oxidation state 3+), and to $ZnIr_2O_4$ (formal oxidation state 3+). All these materials were modelled in their common reported structures: tetragonal (space group $P4_2/mn$, rutile structure) for IrO_2, rhombohedral (space group $R\bar{3}c$, corundum structure) for Ir_2O_3, and cubic (space group $Fd\bar{3}m$, spinel structure) for $ZnIr_2O_4$. To the best of our knowledge, the preparation of single-crystal Ir_2O_3 is not yet reported. However, its presence in IrO_2 powders was discussed in[25,26], and corundum Ir_2O_3 (001) surface oxide was synthesized at high oxygen pressure[27] in the oxidation of Ir (111) surface. Besides, several papers describe and report measurements of properties of devices based on corundum-structured Ir_2O_3, although without discussing the actual structure of the material[28,29].

Our DFT calculations are based on the method of linear combination of atomic orbitals (LCAO). We use atom-centered basis sets (BS) of Gaussian-type functions adopted from the literature. The relativistic effective core pseudopotential with 60 core electrons[30] and basis set of triple-zeta valence with f-polarization function[30,31] for Ir were taken from the Basis Set Exchange resource[32] and earlier used by Ping et al.[33]. All-electron BSs for O and Zn were taken from[33] and Gryaznov et al[34], respectively. We modified the basis set for Zn by optimizing exponent values of the two most diffuse orbitals: one from *sp* series and one from *d* series (see SI for details). We optimized these values with respect to the total electronic energy of the system with constant volume and atomic positions. The convergence limit of this procedure, based on the Powell's conjugate direction method and used as implemented in the OPTBAS[35] interface to CRYSTAL was set to 10^{-5} a.u. For all other calculations, the convergence limit on the total energy for the self-consistent field procedure was set to 10^{-7} a.u. for both electronic and lattice structure relaxation.

As the exchange-correlation functional we chose hybrid PBE0 functional with 25% of Hartree-Fock exchange[36]. We should mention that the bandgap value of pure ZnO obtained in the present calculations with the PBE0 functional is 3.45 eV, a value that is reasonably close to the experimental value of 3.44 eV[37] and which did not require an increase of the amount of exact exchange suggested in the literature for the HSE functional[38]. Indeed, our test calculation with the HSE functional showed band gap of 2.93 eV, suggesting that this effect is basis-independent. The Brillouin zone was sampled with either 4×4×4 (for the L4 supercell) or a 2×2×2 (L48) Γ-centered k-point mesh generated with the Monkhorst-Pack[39] method. All calculations of defective structures in the neutral supercells were spin-polarized and did not include the spin-orbit effects; the use of symmetry operations was explicitly omitted. Computational parameters (the choice of basis sets, functional and integration precision) have been validated to faithfully represent the bulk properties of ZnO, IrO_2 and Ir_2O_3, and $ZnIr_2O_4$.

O_i incorporation energy

As discussed above IrO_x complexes with n exceeding 2 are not obtainable in the wurtzite structure by simply substituting Zn with Ir. The number of oxygen neighbours for each cation in the wurtzite structure is 4. Therefore, the additional O_i atoms are required. Thus, in our calculations for the $Ir^{3+}O_4$, $Ir^{4+}O_5$ and $Ir^{4+}O_6$ complexes defective L4 supercells contain 18 ions (8 metals and 10 oxygens) meaning two O_i's were added. The large supercell L48, containing 194 ions (96 metals and 98 oxygens) was used for the $Ir^{4+}O_6$ only. Optimization of atomic positions in defective supercell may lead to very different atomic configurations; therefore, energetic criteria are important for their comparison. To compare systems of different atomic configurations we use the so-called incorporation energy, calculated from total electronic energies:

$$E_{inc}(O_i) = E(O_i) - E(Ir) - E(O_2), (1)$$

where $E(O_i)$ is the total electronic energy of the supercell with two O_i atoms and with an Ir atom, $E(Ir)$ is the total electronic energy of the supercell with $Ir^{2+}O_4$ and without O_i, $E(O_2)$ is the total electronic energy of an oxygen molecule. The incorporation energies were successfully introduced to analyze the stability of fission products at different pre-existing trap sites in UO_2[40]. Pre-existing trap sites may include vacancies and interstitials. In the case of interstitial sites, the incorporation energy coincides with the solution energies being different by the formation energy of the trap site. A negative value of incorporation energy means that incorporation is energetically favourable. All total electronic energies in Eq.1 are calculated using the same basis set and exchange-correlation functional. The results of $E_{inc}(O_i)$ as discussed below correspond to the concentration of Ir c=12.5% (L4) only.

Calculation of thermoelectric properties

CRYSTAL17 allows to post-process DFT wavefunctions for evaluating the electron transport properties by solving the Boltzmann equation. Unlike other approaches implemented in popular codes such as BoltzTrap[41] or BoltzWann[42], CRYSTAL17 performs analytical derivatives of the electronic bands. Several studies have shown that all these codes, despite their differences, yield similar results[43,44]. At the core of the equations for the transport coefficients (such as Seebeck coefficient and electronic conductivity) is the transport distribution function, cast here as the energy projected tensor:

$$\Xi_{qr}(E) = \tau \sum_k \frac{1}{N_k} \frac{1}{V} \sum_{i,j} v_{i,q}(k) v_{j,r}(k) \delta(E - E_i(k)), (2)$$

where N is the number of k-points used in sampling the reciprocal space, $v_{i,q}(k)$ is the velocity of the ith (j^{th}) band calculated along the direction q (r), δ is an approximation to Dirac's delta function, and τ is electronic relaxation time which is assumed to be not dependent on k (constant relaxation time approximation). Relaxation time is temperature-dependent and cannot be obtained from *first-principles* calculations, and, therefore, must be either fitted or obtained experimentally[20,43]. Throughout our calculations, we have used τ = 10 fs, which is a conservative estimate for a system leaning towards conductivity. Values of τ for ZnO, calculated from mobility data found in literature, range from 17 to 57.9 fs for carrier concentrations ca. ~10^{16} cm^{-3}.[45,46]

By integrating the conductivity distributions written with tensors of eq. 2, it is possible to obtain conductivity tensors, for instance, the electrical conductivity σ:

$$\sigma_{qr}(T;\mu) = e^2 \int dE \left(-\frac{\partial f_0}{\partial E}\right) \Xi_{qr}(E), (3)$$

where μ is the chemical potential or Fermi level, E is the energy, f_0 is the Fermi-Dirac distribution, and T is the temperature. Thermoelectric coefficient σS, where the Seebeck coefficient S is cast as:

$$[\sigma S]_{qr}(T;\mu) = \frac{e}{T} \int dE \left(-\frac{\partial f_0}{\partial E}\right)(E-\mu)\Xi_{qr}(E). (4)$$

For convenience, we use the Fermi level $\mu_F = \mu - E_{VBM}$ for the analysis of main results, where E_{VBM} is the valence band maximum. The transport coefficients were calculated in CRYSTAL with the Fermi level step (parameter to MURANGE) equal to 0.1 eV and the energy step (parameter to TDFRANGE) of 0.05 eV for the supercell L4 (c=12.50%). Notice that the same parameters should be chosen with caution for the supercell L48 (c=1.04%). Our careful treatment of these parameters for L48 suggested both the Fermi level step and the energy step should equal to 0.05 eV.

Results and discussion
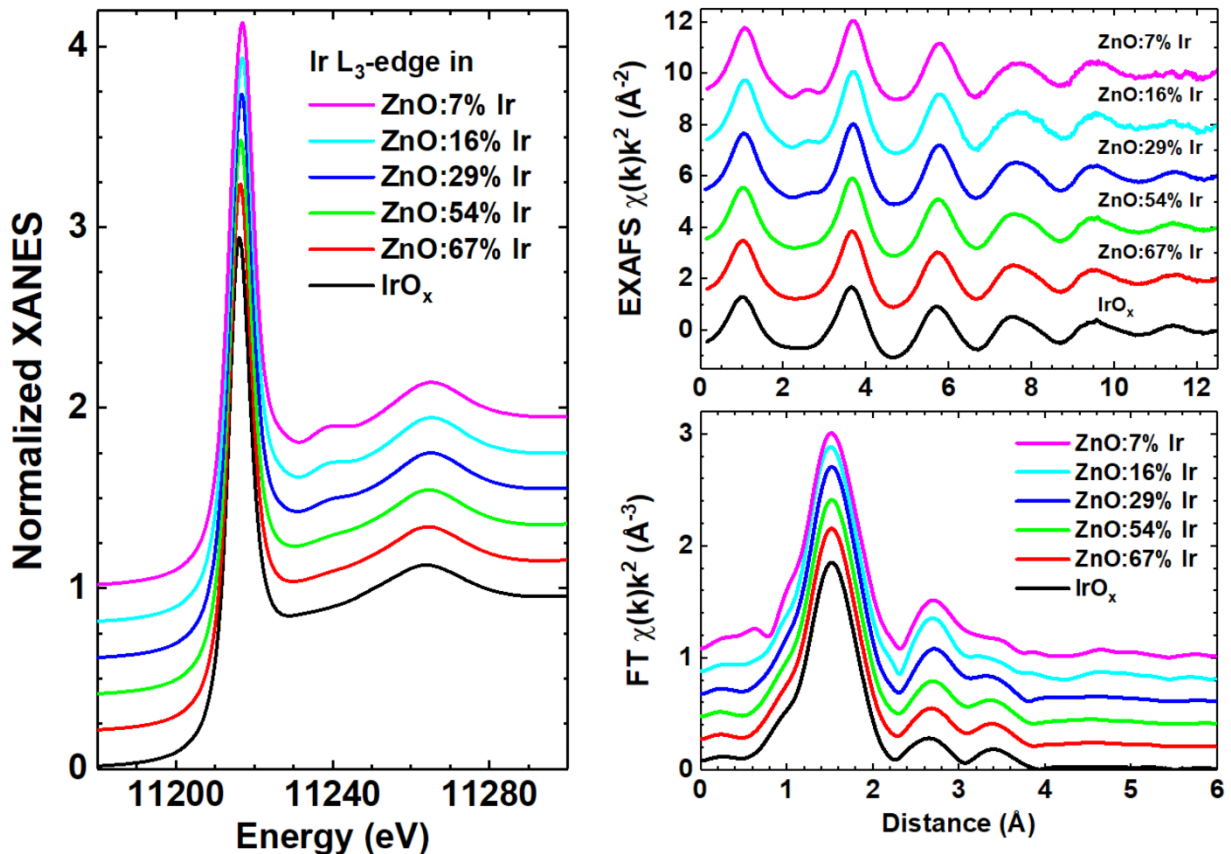
Structural properties of synthesized samples

Figure 1. Experimental Ir L₃-edge XANES (left panel), EXAFS and their Fourier transforms (FT) (right panel) for mixed zinc-iridium oxide (ZnO:cIr) and pure IrOₓ thin films.
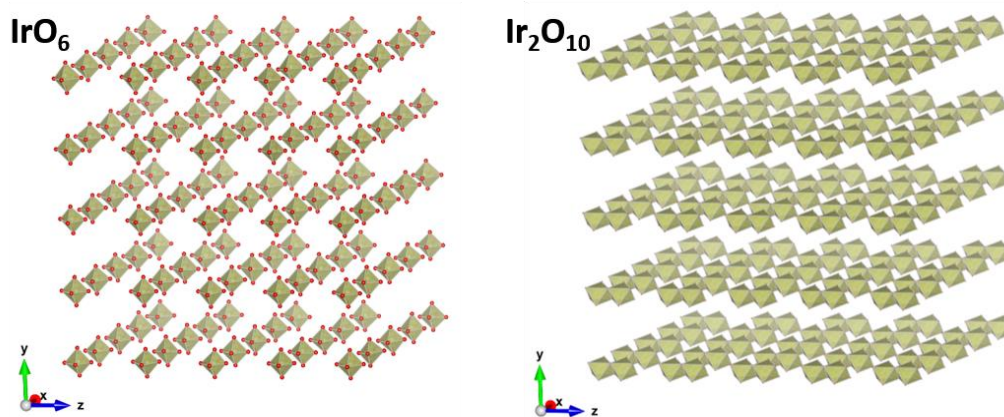
Figure 2. Two 5×5×5 supercell models used in the RMC simulations and composed of single IrO_6 octahedra (left) and groups of two IrO_6 octahedra joined by the edge (right).

Careful examination of the experimental EXAFS spectra and their FTs (Fig. 1) suggests that the local environment around iridium atoms is quite disordered, being typical for nanocrystalline or amorphous IrO_x films[47]. Indeed, reliable

structural contributions are present in FTs up to about 4 Å and consist of three peaks: the main peak at 1.5 Å is due to the nearest oxygen atoms of the first coordination shell, while the origin of the next two peaks at 2.5 and 3.5 Å should be
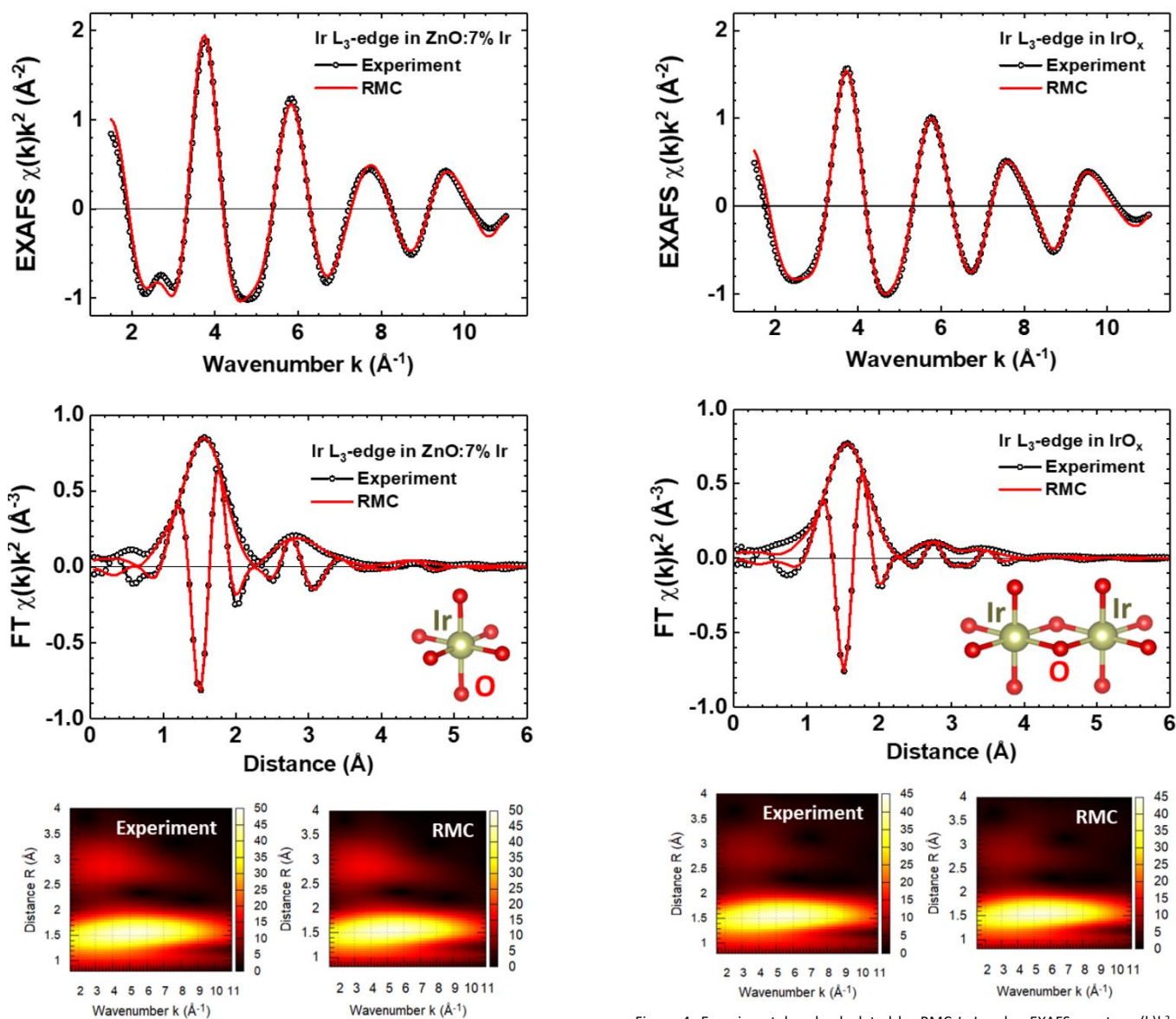

Figure 3. Experimental and calculated by RMC Ir L_3-edge EXAFS spectra $\chi(k)k^2$ and their Fourier and Morlet wavelet transforms for ZnO:7%Ir thin film.

Figure 4. Experimental and calculated by RMC Ir L_3-edge EXAFS spectra $\chi(k)k^2$ and their Fourier and Morlet wavelet transforms for pure IrO_x thin film.

clarified. Our previous experience suggests that in metal oxide thin films such peaks can be due to multiple-scattering (MS) effects within the first coordination shell of the metal atom[48] with additional contributions originating from metal atoms located in the second coordination shell[49]. Thus, the structural model required to describe the local environment of iridium should be cluster-like, i.e. containing a few atoms. Besides, the closeness of the experimental Ir L_3-edge XANES and EXAFS spectra for pure IrO_x and Ir-doped ZnO thin films gives strong evidence for the similarity of their structures. The Ir L_3-edge XANES is dominated by the white line at ~11217 eV due to dipole allowed transition $2p_{3/2}(Ir)\rightarrow 5d(Ir)+2p(O)$[50]. A decrease of the iridium concentration leads to the appearance of the shoulder at 11240 eV, also visible in the EXAFS spectra at 2.5 Å^{-1}: it is due to the damped high-frequency contribution originating from peaks at 2-4 Å in FTs. Thus, all samples can be roughly divided into two groups, having close XANES and EXAFS spectra: the first group with c≤29% and the second group with c≥54% and pure IrO_x.

Crystalline IrO_2 adopts the rutile-type structure (space group $P4_2/mnm$) with slightly distorted (2×1.96 Å and 4×2.00 Å) octahedral coordination of iridium atoms by oxygens[51].

The IrO_6 octahedra are joined by edges along the c-axis direction forming chains, which are cross-linked by shared corners to four neighbouring chains[51]. Therefore, we used different fragments of the rutile IrO_2 structure to construct two structural models for RMC simulations. The first model included a single IrO_6 octahedron, whereas the second model contained two IrO_6 octahedra joined by the edge. In both cases, a 5×5×5 supercell (a simulation box) was constructed (Fig. 2) and used in the RMC/EA simulations to get sufficient statistics from 125 independent structural units (IrO_6 or Ir_2O_{10}). Each iridium-oxygen unit was placed in the centre of the cell with a large enough size (10 Å×10 Å×10 Å) to exclude the influence of units located in the neighbouring cells on each other.

The details of the RMC/EA method were described in[17,18]. The number of simultaneously used atomic configurations in the EA method was 32. At each iteration, the new atomic configuration was generated by randomly displacing all atoms in the simulation box with the maximally allowed shift of 0.4 Å to get the best possible agreement between the Morlet wavelet transforms (WTs) of the experimental and calculated EXAFS spectra $\chi(k)k^2$. The calculations were performed in the k-space range from 1.5 to 11 Å^{-1} and in the R-space range from 0.8 to 4.0 Å. No significant improvement in the residual was observed after 5000 iterations.

The configuration-averaged EXAFS spectra during each RMC/EA simulation were calculated using ab initio real-space multiple-scattering (MS) FEFF8.50L code[52,53], including the MS effects up to 4th order. The scattering potential and partial phase shifts were calculated for each absorption edge only once within the muffin-tin (MT) approximation [52,53] for the cluster with a radius of 5 Å, constructed from rutile IrO_2 structure and centred at the absorbing iridium atom. Small variations of the cluster potential due to atom displacements during the RMC/EA simulations were neglected. The complex

exchange-correlation Hedin-Lundqvist potential was used to account for the photoelectron inelastic losses within the one-plasmon approximation[54]. The amplitude reduction factor S_0^2 was included in the scattering amplitude[52,53], calculated by the FEFF code, and no additional correction of the EXAFS amplitude was performed.

The results of the RMC/EA simulations for two selected samples from each group are reported in Figs. 3 and 4. As one can see, two simple structural models (Fig. 2) provide good agreement with the experimental data, reproducing contributions from all peaks observed in FTs. In ZnO:cIr samples with c≤29%, iridium atoms are octahedrally coordinated by six oxygens with R(Ir-O) = 1.93±0.02 Å and the mean square relative displacement (MSRD) σ^2(Ir-O) = 0.0050±0.0005 Å^2. The group of peaks located at longer distances in FT is solely due to the MS effects within IrO_6 octahedron. In ZnO:cIr samples with c≥54% and pure IrO_x, iridium atoms are also octahedrally coordinated by six oxygens with slightly longer mean bond R(Ir-O) = 1.96±0.02 Å, having slightly larger MSRD σ^2(Ir-O) = 0.0065±0.0005 Å^2. However, there is an additional iridium atom from the neighbouring octahedron located at R(Ir-Ir)= 3.15±0.02 Å with MSRD σ^2(Ir-Ir) = 0.0056±0.0005 Å^2, whose EXAFS, together with that from remaining 4 oxygen atoms, interferes with the MS contribution from the first shell, resulting in the two-peak structure in FT. Thus, at high Ir dopant concentration and in pure IrO_x films, structural groups of two IrO_6 octahedra joined by the edge can be evidenced. These groups form chains in crystalline rutile-type IrO_2[51].

DFT atomic structures of Iridium-oxygen complex in ZnO and parent compounds

We focus our discussion of oxidation state n of Ir in $Ir^{n+}O_x$ complex in ZnO on analogy with "pure" reference compounds: IrO_2, Ir_2O_3, and $ZnIr_2O_4$ (see computational details). In either structure, Ir is six-fold coordinated, and in both IrO_2 and Ir_2O_3 the six neighbouring oxygens are split into two groups (orbits) by symmetry, yielding long (axial) and short (azimuthal) Ir-O distances. The calculated lattice parameters of IrO_2 and $ZnIr_2O_4$ are consistent with experimental data (table S1). Our results show several possible ways to distinguish Ir^{3+} from Ir^{4+} (Table 1). First, the magnetic moment (μ_{Ir}) of Ir demonstrates that Ir in all these oxides is in the low-spin state with electron configurations $5d^5$ (n = 4, IrO_2) and $5d^6$ (n = 3, Ir_2O_3 and $ZnIr_2O_4$). Second, the effective atomic charge of Ir (q_{Ir}), matching different oxidation states, is quite different for these two states, which makes it a useful descriptor for comparing different $Ir^{n+}O_x$ complexes. Thus, the larger (q_{Ir}) in IrO_2 than in Ir_2O_3 and $ZnIr_2O_4$ is in accordance with a larger n in the former. Third, the Ir-O distances are typically longer for Ir^{3+} than for Ir^{4+} in table 1.

The smaller ionic radius of Ir^{4+} leads to a smaller lattice constant in IrO_2 and, therefore, stronger hybridization between the Ir and O electronic states. Interestingly, the bandgap (ΔE) values in Ir_2O_3 and $ZnIr_2O_4$ are quite close. It was discussed earlier that the use of the hybrid exchange-

correlation functional is critical to reproduce the bandgap in $ZnIr_2O_4$[13]. The calculated ΔE for $ZnIr_2O_4$ in the present study is well comparable with the recently obtained experimental data from[55].

In Tables 2 and 3 we present basic properties of the most important configurations of $Ir^{n+}O_x$ complexes, distinguished by the number of surrounding oxygens, incorporation energy

Table 1. Calculated bulk properties of IrO₂, Ir₂O₃, and ZnIr₂O₄. a, c are the lattice parameters, d_{Ir-o} is the Ir-O interatomic distance, $q_{Ir}(\mu_{Ir})$ and $q_O(\mu_O)$ are the effective atomic charges (magnetic moments) of Ir and O, respectively, and ΔE the bandgap value. Extended table (table S1) with experimental data for comparison is present in Supplementary Information.

crystal	d_{Ir-o}, Å	q_{Ir}, e	μ_{Ir}, μB	q_O, e	μ_O, μB	ΔE, eV
IrO₂	short: 1.942 long: 1.999	1.712	0.625	-0.856	0.171	Metal
Ir₂O₃	short: 2.053 long: 2.085	1.241	0.000	-0.827	0.000	3.39
ZnIr₂O₄	2.069	1.067	0.000	-0.824	0.000	3.44

Table 2. Basic properties of $Ir^{n+}O_x$ complexes. d_{Ir-o} is Ir-O interatomic distance, q_{Ir} is the effective atomic charge of Ir, μ_{Ir} is the magnetic moment of Ir. Two supercell sizes were used for the $Ir^{4+}O_6$ complex for comparison, namely L4 and L48. Data obtained for the larger (L48) supercell is given in parentheses. Note that the Zn-O distance in ZnO is 1.98 Å.

Complex	d_{Ir-o}, Å	d_{Ir-o}, Å (avg)	q_{Ir}, e	μ_{Ir}, μB
$Ir^{2+}O_4$	2.136-2.176	2.147	0.751	2.530
$Ir^{3+}O_4$	1.846-1.920	1.885	1.193	1.795
$Ir^{4+}O_5$	1.828-2.024	1.954	1.095	0.695
$Ir^{4+}O_6$	1.893-1.972 (1.892-2.047)	1.938 (1.936)	1.325 (1.366)	0.514 (0.507)

(Eq. 1), oxidation state n, and formation of peroxide fragments (or lack thereof). The main difference between the configurations is due to the number of oxygens surrounding Ir. We, thus, obtain the configurations with the number of surrounding oxygens ranging from 4 to 6, whereas n varies from 2 to 4. The obtained n-values are consistent with the oxidation states analysis for amorphous IrOₓ powders[56]. It was shown in that work that the average oxidation state of Ir is around 3.6 indicating the presence of Ir³⁺ and Ir⁴⁺ in the powders. The Ir oxidation state is 2+ if the interstitial oxygens are absent ($Ir^{2+}O_4$). In this case, d_{Ir-o}, q_{Ir} and μ_{Ir} are obviously different from other oxidation states and configurations in Table 2.

In the case of $Ir^{3+}O_4$ complex, Ir has four neighbors, too, and yet in this case the properties of Ir are not the same as in the $Ir^{2+}O_4$ case. In $Ir^{3+}O_4$, the value of μ_{Ir} corresponds to n = 3 and an intermediate spin state (the formal value of μ_{Ir}= 2 μB). However, d_{Ir-O} in the $Ir^{3+}O_4$ complex differs from that in

Ir₂O₃ and ZnIr₂O₄ (table 1). It is smaller than in the parent oxides whereas q_{Ir} in $Ir^{3+}O_4$ is close to the one of Ir in Ir₂O₃. The other two cases of $Ir^{4+}O_5$ and $Ir^{4+}O_6$ are characterized by small magnetic moments of Ir, consistent with the low spin configuration of the 5d⁵ orbital. Such magnetic moments of Ir are very close to that in IrO₂ (table 1). In contrast to other complexes, the O_i ions are Ir's nearest neighbors in the $Ir^{4+}O_6$ complex, and do not participate in the formation of peroxide defects.

The Ir-O distances are shorter in the complexes containing the O_i ions than in the $Ir^{2+}O_4$ case and parent compounds, which is connected with a greater overlap of the orbitals and results in an increased oxidation state of Ir. The calculated average Ir-O bond length of the $Ir^{4+}O_6$ complex matches experimental data obtained with EXAFS (1.94 Å vs 1.96 Å). Interestingly, the larger supercell (L48) used for the $Ir^{4+}O_6$ complex did not demonstrate any changes in the basic properties (table 1).

Table 3. Incorporation energy ($E_{inc}(O_i)$) of interstitial oxygens O_i (Eq. 1) in the different complexes (suprecell L4 c = 12.5%), d_{O-O} is the O-O interatomic distance, and the local vibrational frequency (ν) of peroxide.

Complex	Peroxide	d_{O-O}, Å	$E_{inc}(O_i)$, eV	ν, cm⁻¹
$Ir^{3+}O_4$	Yes	1.47	-3.77	942
$Ir^{4+}O_5$	Yes	1.54	-4.37	810
$Ir^{4+}O_6$	No	—	-5.15	—

Table 3 indicates that the six-fold coordinated Ir is energetically preferable state, as it is characterized by the lowest energy of incorporation. However, the $Ir^{3+}O_4$ and $Ir^{4+}O_5$ complexes contain the peroxide defects, formed by one O_i ion and one host oxygen ion. The interatomic distances (d_{O-O}) between these two oxygens are consistent with the values known for this type of defect (dumbbell) in other materials and ZnO from the DFT calculations[11,57–59].

From the experiment viewpoint, the O-O bond in O_2^{2-} has been reported to have a length varied from 1.47 to 1.54 Å for Ir(O₂) complexes in organic compounds[60–62]. Stretching vibration of the O-O bond has been assigned[62] an IR absorption band at ν=833 cm⁻¹. Likewise, d_{O-O} of 1.47 Å has been reported for a cubic zinc peroxide (ZnO₂)[63]. In the latter study, authors have observed a strong Raman peak centred at 835 cm⁻¹, which they attribute to the O-O stretching vibration through comparison with other published data[64,65]. However, a larger calculated d_{O-O} equal to 1.75 Å for ZnO₂ was associated with the experimentally measured ν of 748 cm⁻¹ taken from the literature (see[66] and references therein). Importantly, the present calculated ν's of peroxide defect are only slightly larger than the measured one of 720 cm⁻¹ for Ir-doped ZnO[10].
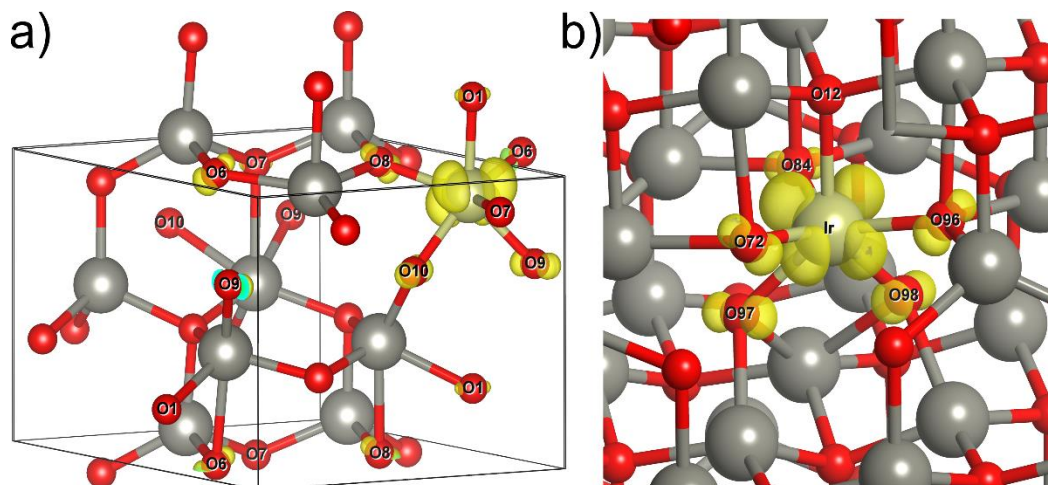
Analysis of the electronic structure

Figure 5. The atomic structure and spin-density distribution in the smaall L4 (a) and large L48 (b) supercell for the $Ir^{4+}O_6$ complex. Light yellow spheres represent Ir atoms, gray – Zn, and red – O atoms. Yellow clouds represent orbitals with unpaired electrons. Teal clouds are the same orbitals sectioned by the periodic boundary. The box marks the supercell boundaries. All named oxygen atoms are bound to Ir and have a nonzero spin.

Even without O_i's, Ir induces a non-zero spin on neighbouring oxygen ions in the $Ir^{2+}O_4$ complex. The magnetic moment of its 4 O neighbours varies from 0.10-0.12 μ_B. Such values of the magnetic moment are of the same order as those for the oxygens surrounding Ir in the complexes with O_i's. This is also well demonstrated by the spin density distribution shown in figs. S1a-c and fig. 5. The maximum spin density is localized on Ir whereas there is some part of the spin density on the nearest oxygen neighbours. A non-zero spin of oxygen ions surrounding Ir and the fact that these ions have a decreased charge (not shown) in comparison with other oxygen ions are very much in line with the same properties of IrO_2 in contrast to Ir_2O_3 and $ZnIr_2O_4$ (table 1). Ir is fully oxidized, and the electrons given to surrounding oxygens are distributed between them, including O_i's. It facilitates hole localization in Ir-doped ZnO. Interestingly, in the case of peroxide defect, the resultant fragment is asymmetric, with different magnetic moments of the two oxygens. Notice, however, that the magnetic moments of oxygens in O_2^{2-} are more pronounced in the $Ir^{4+}O_5$ complex than in the $Ir^{3+}O_4$ one due to the smaller O-O distance in the former case.

Analysis of the calculated density of states (DOS) for the $Ir^{4+}O_6$ complex (fig. 6 and fig. 7c) revealed that the top of the valence band consists of Ir states and states of oxygens surrounding Ir (Ir-O band). It is the band of the width of ~0.4 eV (small supercell, L4). The states of the same oxygens are extended to deeper energies and hybridized with the states of other oxygens in the lattice (the total width of this band is around 5 eV). The Zn states contribute at even deeper energies. In the large supercell (L48 fig. 7d), the Ir-O band is separated from the extended O-band which should have an impact on the calculated thermorelectric properties. The band
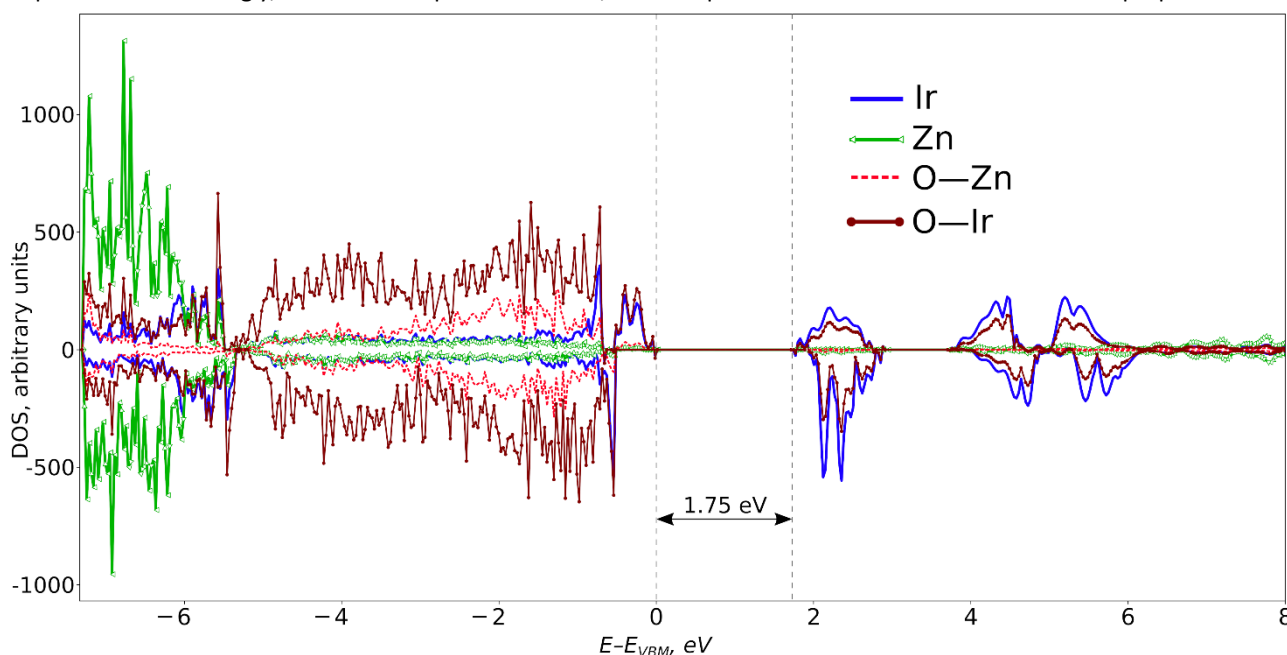

Figure 6. Total and partial density of states (DOS) for $Ir^{4+}O_6$ calculated with the small supercell (L4). The O-Ir line describes the 6 oxygens surrounding Ir, whereas O-Zn line is for all the other oxygens in the supercell. The valence band maximum (E_{VBM}) is taken as zero. Negative DOS values correspond to the spin-down electrons. Signals of Ir, O-Zn, and O-Ir are scaled by factors of 10, 3, and 5 respectively.

gap in Ir-doped ZnO is between the occupied and unoccupied Ir-O bands and changes from 1.75 to 2.50 eV for the small (L4, c = 12.50%) and large (L48, c = 1.04%) supercell.

Even though the overall characteristics in the calculated complexes are similar, there are still some differences to mention (fig. S2 and fig. 7b). The hybridization effect as discussed above is stronger in $Ir^{3+}O_4$ than in $Ir^{4+}O_6$. Essentially, the top of the valence band in $Ir^{3+}O_4$ is formed of Ir states and all oxygens in the lattice. In the case of $Ir^{4+}O_5$ complex, the picture is similar with $Ir^{4+}O_6$ but the Ir-O band is wider (almost 1 eV).

Analysis of thermoelectric properties

In the present analysis, we discuss the calculated thermoelectric properties, i.e. the Seebeck coefficient (S) and electrical conductivity (σ), for the IrOₓ complexes in ZnO and reference systems: perfect ZnO, $ZnIr_2O_4$ and IrO_2. Thermoelectric properties are extremely sensitive to the electronic structure. Perfect ZnO is not expected to demonstrate good potential for the p-type conduction. We suggest that this property of ZnO is reflected in the steep increase of the calculated S to unrealistically high values (see fig. S2a) in the proximity of VBM.

In the calculations the exact Fermi level μ_F is unknown but a comparison with the available experimental data could help with its identification. Therefore, S and σ dependence on μ_F referenced at the VBM, i.e. S(μ_F) and σ(μ_F), lies at the heart of our analysis. Typically, such dependencies have two parts for positive and negative values of S standing for holes and electrons, respectively. We, therefore, focus our analysis on the positive S-values only to estimate the potential of Ir-doped ZnO for the p-type conduction.

In Table 4 the calculated σ- and S-values at fixed μ_F are compared with the corresponding data found in the experimental literature and our previous experimental results[10]. Notice that the experimental results differ by the sample preparation and treatment, leading to some scatter in data. Interestingly, it is almost the same value of $\mu_F = \mu - E_{VBM} \approx$ 0.7 eV for all systems for both S and σ in table 4 to find better correspondence with the experimental values and is, therefore, a good compromise for such a comparison.

The calculated σ-value for $ZnIr_2O_4$ and IrO_2 agree very well with the experimental data. The cation vacancies and anti-sites are detrimental defects in spinels[13,67] explaining, at least in part, the p-type conductivity. Thus, it should be reflected in the S-values as well. Indeed, we emphasize significant differences in the behaviour of S(μ_F) for bulk $ZnIr_2O_4$ in a comparison with perfect ZnO. It has a well distinguished

plateau in the range of μ_F between 0 and 0.8 eV (fig. 7a) followed by a steep increase to very high values. A positive Seebeck coefficient of 92.3 μVK⁻¹ at μ_F = 0.7 eV is in agreement with the experimental values (Table 4).

The Ir-doped ZnO is characterized by a high sensitivity of thermoelectric properties to the electronic structure as well. All IrOₓ complexes as discussed in the present study show different behaviour of S(μ_F). However, we again emphasize the presence of plateau and steep increase to very high values for some of the complexes. The positive Seebeck coefficient is in the range 60-80 and 55-90 μVK⁻¹ for the complex without the interstitial oxygens, ($Ir^{2+}O_4$), and in the $Ir^{4+}O_6$ complex in the small supercell (c=12.5%, L4), respectively, depending on μ_F (in the range of μ_F between 0 and 0.8 eV) at 308 °K. Neither the $Ir^{2+}O_4$ nor $Ir^{4+}O_6$ complex in the small supercell (L4) are characterized by the steep increase of S(μ_F) as were found in perfect ZnO and $ZnIr_2O_4$. Here S(μ_F) increases smoothly approaching the maximum value at $\mu_F \sim$ 0.70-0.75 eV (fig. 7 b,c). In contrast, the $Ir^{4+}O_5$ and $Ir^{3+}O_4$ complexes (fig. S2) show very similar behavior of S(μ_F) with $ZnIr_2O_4$ and demonstrate much smaller changes for the S-values in the range of μ_F between 0 and 0.8 eV. In figs. S2b,c it is demonstrated that the plateau in the range of μ_F between 0 and 0.8 eV is present and leads to the values of S of the order of ~89 μVK⁻¹ (see also table 4). The presence of plateau and formation of O_2^{2-} are, in our opinion, interconnected.

We do not expect perfect agreement for the absolute S-values between the experiment and simplified model in the calculation but rather present a qualitative picture explaining the p-type conduction in Ir-doped ZnO. Also, we notice a significant decrease of σ for the Ir concentration c=1.04% ($Ir^{4+}O_6$, L48). In this case there is again the steep increase of the calculated S to very high values (see fig. 7d) in the proximity of VBM similar to perfect ZnO. In the complexes with the plateau the steep increase is shifted to higher μ_F. At the values of μ_F = 0.8 -1.9 eV for $Ir^{3+}O_4$ and 0.8-1.6 for $Ir^{4+}O_5$ the steep increase of S is observed and transformation into the n-type conductor follows. Furthermore, S(μ_F) is differently influenced by temperature T in the two ranges of μ_F, 0.0<μ_F≤0.8 eV and 0.8<μ_F≤1.9(1.6) eV, in figs. 7 (f,g,h) and figs. S2 (d,e). At $\mu_F \leq$ 0.8 eV, S(μ_F) increases with T, and an opposite behaviour is found in the range 0.8<μ_F≤1.9(1.6) eV for the complexes with the steep increase. Qualitatively speaking, this picture is very close to what was observed for $ZnIr_2O_4$ as well (fig. 7e).

Table 4. Calculated thermoelectric properties. S is the Seebeck coefficient, σ is the electrical conductivity and c the Ir concentration. Only the maximal component of the S tensors are given for the Fermi level $\mu_F=\mu-E_{VBM}$ = 0.7 eV). All the calculated and measured properties are given at 308 $^\circ$K, if not otherwise stated.

Compound	S, µVK^{-1}	S exp, µVK^{-1}	σ, Ω^{-1}m^{-1}	σ exp, Ω^{-1}m^{-1}
ZnO	2510	Non-conducting	6.05×10^{-8}	Non-conducting
ZnIr$_2$O$_4$	92.3	53.9[a][68]	1.72×10^2	2.09×10^2, $3.39\times10^{2\,[a][68]}$
IrO$_2$	63.9	-	1.32×10^6	$1.15–2.90\times10^{6\,[69,70]}$ $0.68-1.67\times10^{6\,[b][71]}$ $2.94\times10^{6\,[c][71]}$
Ir$_2$O$_3$	105	-	8.98×10^1	-
$Ir^{2+}O_4$	80.1		2.57×10^2	
$Ir^{3+}O_4$	88.7		3.20×10^1	
$Ir^{4+}O_5$	89.4	6.8[d][10]	4.13×10^1	47.6[d][10]
$Ir^{4+}O_6$ (c=12.5%, L4)	83.8		1.62×10^2	
$Ir^{4+}O_6$ (c=1.04%, L48)	2335		3.49×10^{-8}	

Notes: a) measured at room temperature; two values for σ for polycrystalline and epitaxial thin films whereas the Seebeck coefficient was measured for polycrystalline films only; the thin films prepared by PLD between 773 and 973 $^\circ$K b) the values are taken at room temperature for the 100 nm thin films prepared by PLD and oxidized at 0.05-0.2 mBar and 500 $^\circ$C; c) the bulk value measured at room temperature d) the Ir concentrations c = 16.4%.
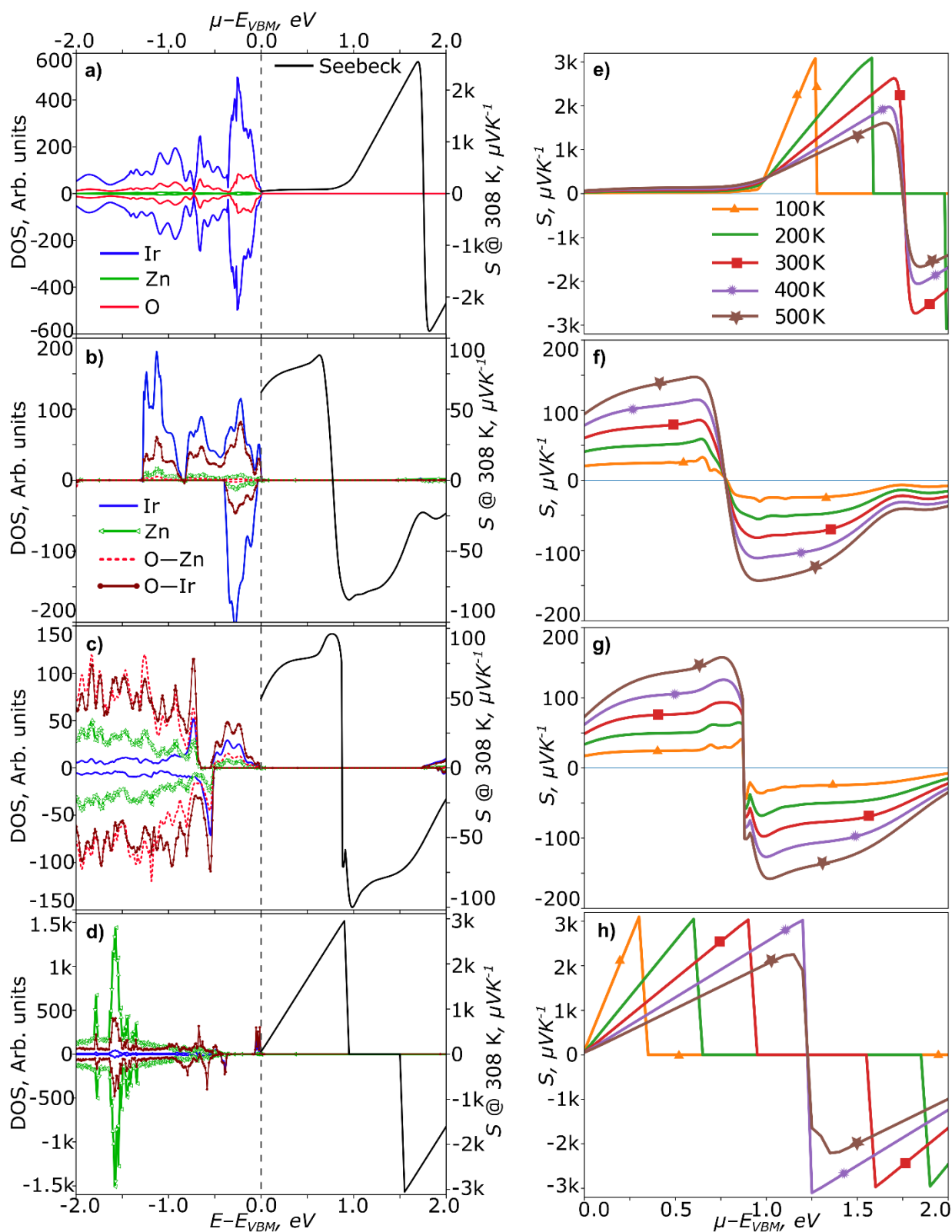
Figure 3. Left panel: The partial DOS as a function of E- E_{VBM} (left-bottom axis) and Seebeck coefficient (S, black curve) at T=308 °K as a function of Fermi level $\mu_F = \mu$-E_{VBM} (top-right axis). The valence band maximum (E_{VBM}) is taken as zero (grey dashed line). DOS lines are smoothed with a cubic spline. No scaling is applied. Right panel: S(μ_F) for a range of temperatures. ZnIr$_2$O$_4$: (a) and (e), $Ir^{2+}O_4$: (b) and (f), $Ir^{4+}O_6$ in L4: (c) and (g), $Ir^{4+}O_6$ in L48: (d) and (h). The O-Ir line describes the oxygens surrounding Ir, whereas O-Zn line is for all the other oxygens in the supercell.

Conclusions

We have successfully combined hybrid DFT calculations and Ir L_3-edge XAS experiments to get insight into the local atomic structure around iridium ions in Ir-doped ZnO. The ZnO:cIr (c=7%, 16%, 29%, 54% and 67%) and IrO_x thin films of the thickness 200-300 nm were deposited by reactive DC magnetron co-sputtering on polyimide tape substrates. The role of interstitial oxygens was emphasized in such experiments. Thus, the analysis of EXAFS spectra using the reverse Monte Carlo simulations revealed that iridium ions are predominantly octahedrally coordinated by oxygens. Consequently, several IrO_x (x = 4-6) polyhedra (complexes) inside the wurtzite ZnO lattice were selected for the calculations of the atomic and electronic structure, vibrational and thermoelectric properties from the first principles.

The hybrid PBE0 exchange-correlation functional and Gaussian basis-set described very well the basic properties of ZnO, $ZnIr_2O_4$, and IrO_2 crystals, which justified further computational study of Ir-doped ZnO. The complexes ($Ir^{n+}O_x$) were distinguished by the oxidation state of Ir (n) and formation of peroxide defects, and as a consequence, by the different number of oxygens (x) surrounding Ir ions. Their corresponding formulas were chosen as $Ir^{2+}O_4$ – the system without interstitial oxygens O_i's, $Ir^{3+}O_4$ – the first system with the interstitials and formation of peroxide defects O_2^{2-}, $Ir^{4+}O_5$ – the second system with the formation of peroxide defect , and lastly, $Ir^{4+}O_6$ the system with Ir ions which are octahedrally coordinated by oxygens. It is worth mentioning that the selected complexes containing two interstitial O_i ions were found by a careful treatment of numerous spatial configurations with different total energies. However, we were able to choose the three most important ones and focus our study on the analysis of the relevant Seebeck coefficient, electrical conductivity and density of states for them. Moreover, the $Ir^{4+}O_6$ complex was calculated with two Ir concentrations, namely 12.50 and 1.04%. We compared the calculated thermoelectric properties for the chosen complexes with those for the reference systems, i.e. perfect ZnO, $ZnIr_2O_4$, and IrO_2. Each calculated IrO_x complex demonstrated some differences in the calculated DOS. However, the main DOS feature of calculated complexes for the Ir concentration 12.5% is due to 1) the mixed Ir-O band contributing to the VBM 2) the states of oxygens surrounding Ir and their extension and hybridization with the other oxygens states in the lattice 3) and, as a consequence, the predicted positive Seebeck coefficient and electrical conductivity for the Fermi level μ_F (referenced at the VBM) lying in the range $0 \leq \mu_F \leq 0.8$ eV. In this μ_F-range the calculated Seebeck coefficients are close for the four calculated complexes including the one without O_i's. In contrast, the calculation of smaller Ir concenctration (1.04%) for the $Ir^{4+}O_6$ complex revealed the Seebeck coefficient behaviour similar with the hypothetical perfect ZnO which is reflected in its steep increase in the proximity of VBM. It can be explained by a separate Ir-O band characterized by much weaker hybridization effect with the host oxygens and smaller width in a comparison with the lager concentration 12.5%.

Such differences between the Ir concentrations should explain the sign change in the Seebeck coefficient behaviour observed experimentally in Ref. 10. Lastly, the calculated local vibrational frequencies of O_2^{2-} peroxides entering two complexes, $Ir^{3+}O_4$ and $Ir^{4+}O_5$, are close to those in the Raman measurements in Ref. 10. The complexes with the formation of peroxide defects, i.e. $Ir^{3+}O_4$ ($Ir^{4+}O_5$), have also the steep increase of Seebeck coefficient in the range $0.8 < \mu_F \leq 1.9(1.6)$ eV similarly with $ZnIr_2O_4$.

Author Contributions

A. C.: Investigation, Formal analysis, Writing – original draft, Visualization. D. G.: Methodology, Writing – review & editing. N. V. S.: Project administration, Supervision. E. A. K.: Project administration, Supervision. A. Z.: Investigation, M. Z.: Investigation. A. K.: Investigation, Formal analysis, Writing – review & editing, Visualization. A. A.: Investigation. J. P.: Funding acquisition.

Conflicts of interest

There are no conflicts to declare.

Acknowledgements

References

1 P. Novák, T. Kozák, P. Šutta, M. Kolega and O. Bláhová, *Phys. Status Solidi A Appl. Mater. Sci.*, 2018, **215**, 1700951.

2 P. Novák, J. Očenášek, T. Kozák and J. Savková, *Thin Solid Films*, 2018, **660**, 471–476.

3 J. Rezek, P. Novák, J. Houška, A. D. Pajdarová and T. Kozák, *Thin Solid Films*, 2019, **679**, 35–41.

4 D. C. Look, B. Claflin, Ya. I. Alivov and S. J. Park, *Phys Status Solidi A*, 2004, **201**, 2203–2212.

5 A. Janotti and C. G. Van de Walle, *Rep. Prog. Phys.,* 2009, **72**, 126501.

6 D. Mora-Fonz and A. L. Shluger, *Phys. Rev. B*, 2019, **99**, 014202.

7 A. V. Uklein, V. V. Multian, G. M. Kuz'micheva, R. P. Linnik, V. V. Lisnyak, A. I. Popov and V. Ya. Gayvoronsky, *Opt. Mat.*, 2018, **84**, 738–747.

8 S. Lany, J. Osorio-Guillén and A. Zunger, *Phys. Rev. B*, 2007, **75**, 241203.

9   A. Kuzmin and J. Chaboy, *IUCrJ*, 2014, **1**, 571–589.

10 M. Zubkins, R. Kalendarev, J. Gabrusenoks, A. Plaude, A. Zitolo, A. Anspoks, K. Pudzs, K. Vilnis, A. Azens and J. Purans, *Thin Solid Films*, 2017, **636**, 694–701.

11 P. Erhart, A. Klein and K. Albe, *Phys. Rev. B*, 2005, **72**, 085213.

12 D. Muñoz Ramo and P. D. Bristowe, *J. Phys.: Condens. Matter.*, 2016, **28**, 345502.

13 D. M. Ramo and P. D. Bristowe, *J. Chem. Phys.*, 2014, **141**, 084704.

14 D. Muñoz Ramo and P. D. Bristowe, *Thin Solid Films*, 2014, **555**, 112–116.

15 S. Belin, V. Briois, A. Traverse, M. Idir, T. Moreno and M. Ribbens, *Phys. Scr.*, 2005, 980.

16 A. Kalinko, *XAESA*, https://github.com/aklnk/xaesa, 2020.

17 J. Timoshenko, A. Kuzmin and J. Purans, *Comp. Phys. Commun.*, 2012, **183**, 1237–1245.

18 J. Timoshenko, A. Kuzmin and J. Purans, *J. Phys.: Condens. Matter*, 2014, **26**, 055401.

19 R. Dovesi, A. Erba, R. Orlando, C. M. Zicovich-Wilson, B. Civalleri, L. Maschio, M. Rérat, S. Casassa, J. Baima, S. Salustro and B. Kirtman, *WIREs Comput. Mol. Sci.*, 2018, **8**, e1360.

20 R. Dovesi, V. R. Saunders, C. Roetti, R. Orlando, C. M. Zicovich-Wilson, F. Pascale, B. Civalleri, K. Doll, N. M. Harrison, I. J. Bush, P. D'Arco, M. Llunell, M. Causà, Y. Noël, L. Maschio, A. Erba, M. Rerat and S. Casassa, *CRYSTAL17 User's Manual*, University of Torino, Torino, 2017.

21 F. Pascale, C. M. Zicovich-Wilson, F. López Gejo, B. Civalleri, R. Orlando and R. Dovesi, *J. Comp. Chem.*, 2004, **25**, 888–897.

22 C. M. Zicovich-Wilson, F. Pascale, C. Roetti, V. R. Saunders, R. Orlando and R. Dovesi, *J. Comp. Chem.*, 2004, **25**, 1873–1881.

23 R. A. Evarestov, *Quantum chemistry of solids: LCAO treatment of crystals and nanostructures*, Springer, Berlin ; New York, Second edition., 2012.

24 M. Nič, J. Jirát, B. Košata, A. Jenkins and A. McNaught, Eds., *IUPAC Compendium of Chemical Terminology: Gold Book*, IUPAC, Research Triangle Park, NC, 2.1.0., 2009.

25 M. Peuckert, *Surf. Sci.*, 1984, **144**, 451–464.

26 M. Hara, K. Asami, K. Hashimoto and T. Masumoto, *Electrochimica Acta*, 1983, **28**, 1073–1081.

27 W.-H. Chung, D.-S. Tsai, L.-J. Fan, Y.-W. Yang and Y.-S. Huang, *Surf. Sci.*, 2012, **606**, 1965–1971.

28 S. Kan, S. Takemoto, K. Kaneko, I. Takahashi, M. Sugimoto, T. Shinohe and S. Fujita, *Appl. Phys. Lett.*, 2018, **113**, 212104.

29 S. Kan, S. Takemoto, K. Kaneko, T. Shinohe and S. Fujita, in *2018 IEEE CPMT Symposium Japan (ICSJ)*, IEEE, Kyoto, 2018, pp. 95–98.

30 P. J. Hay and W. R. Wadt, *J. Chem. Phys.*, 1985, **82**, 299–310.

31 A. W. Ehlers, M. Böhme, S. Dapprich, A. Gobbi, A. Höllwarth, V. Jonas, K. F. Köhler, R. Stegmann, A. Veldkamp and G. Frenking, *Chem. Phys. Lett.*, 1993, **208**, 111–114.

32 B. P. Pritchard, D. Altarawy, B. Didier, T. D. Gibson and T. L. Windus, *J. Chem. Inf. Model.*, 2019, **59**, 4814–4820.

33 Y. Ping, G. Galli and W. A. Goddard, *J. Phys. Chem. C*, 2015, **119**, 11570–11577.

34 D. Gryaznov, E. Blokhin, A. Sorokine, E. A. Kotomin, R. A. Evarestov, A. Bussmann-Holder and J. Maier, *J. Phys. Chem. C*, 2013, **117**, 13776–13784.

35 R. A. Evarestov, A. I. Panin, A. V. Bandura and M. V. Losev, *J. Phys.: Conf. Ser.*, 2008, **117**, 012015.

36 C. Adamo and V. Barone, *J. Chem. Phys.*, 1999, **110**, 6158–6170.

37 C. M. Bertoni, G. Cappellini, F. Finocchi, P. Monachesi, G. Chiarotti and P. Chiaradia, *7.3.3 II-VI compound surfaces: Datasheet from Landolt-Börnstein - Group III Condensed Matter · Volume 45A: "Physics of Solid Surfaces" in SpringerMaterials*, Springer-Verlag Berlin Heidelberg.

38 F. Oba, M. Choi, A. Togo, A. Seko and I. Tanaka, *J. Phys. Condens. Matter*, 2010, **22**, 384211.

39 H. J. Monkhorst and J. D. Pack, *Phys. Rev. B*, 1976, **13**, 5188–5192.

40 R. W. Grimes and C. R. A. Catlow, *Philos. Trans. R. Soc. A*, 1991, **335**, 609–634.

41 G. K. H. Madsen and D. J. Singh, *Comput. Phys. Commun.*, 2006, **175**, 67–71.

42 G. Pizzi, D. Volja, B. Kozinsky, M. Fornari and N. Marzari, *Comput. Phys. Commun.*, 2014, **185**, 422–429.

43 G. Sansone, A. Ferretti and L. Maschio, *J. Chem. Phys.*, 2017, **147**, 114101.

44 J. Linnera, G. Sansone, L. Maschio and A. J. Karttunen, *J. Phys. Chem. C*, 2018, **122**, 15180–15189.

45 Ü. Özgür, Ya. I. Alivov, C. Liu, A. Teke, M. A. Reshchikov, S. Doğan, V. Avrutin, S.-J. Cho and H. Morkoç, *J. Appl. Phys.*, 2005, **98**, 041301.

46 S. Jantrasee, S. Pinitsoontorn and P. Moontragoon, *J. Electron. Mater.*, 2014, **43**, 1689–1696.

47 A. Kuzmin, R. Kalendarev, J. Purans, and D. Pailharey, in *Advanced Optical Devices, Technologies, and Medical Applications*, 2003, vol. 5123.

48 A. Kuzmin and R. Grisenti, *Phil. Mag. B*, 1994, **70**, 1161–1176.

49 J. Gaidelene, R. Kalendarev, A. Kuzmin and J. Purans, *Nucl. Instrum. Methods Phys. Res. A*, 2004, **531**, 321–326.

50 A. Balerna, E. Bernieri, E. Burattini, A. Kuzmin, A. Lusis, J. Purans and P. Cikmach, *Nucl. Instrum. Methods Phys. Res. A*, 1991, **308**, 240–242.

51 A. A. Bolzan, C. Fong, B. J. Kennedy and C. J. Howard, *Acta Crystallogr. B Struct. Sci*, 1997, **53**, 373–380.

52 A. L. Ankudinov, B. Ravel, J. J. Rehr and S. D. Conradson, *Phys. Rev. B*, 1998, **58**, 7565–7576.

53 J. J. Rehr and R. C. Albers, *Rev. Mod. Phys.*, 2000, **72**, 621–654.

54 L. Hedin and B. I. Lundqvist, *J. Phys. C*, 1971, **4**, 2064–2083.

55 M. J. Wahila, Z. W. Lebens-Higgins, A. J. Jackson, D. O. Scanlon, T.-L. Lee, J. Zhang, K. H. L. Zhang and L. F. J. Piper, *Phys. Rev. B*, 2019, **100**, 085126.

56 V. Pfeifer, T. E. Jones, J. J. Velasco Vélez, C. Massué, R. Arrigo, D. Teschner, F. Girgsdies, M. Scherzer, M. T. Greiner, J. Allan, M. Hashagen, G. Weinberg, S. Piccinin, M. Hävecker, A. Knop-Gericke and R. Schlögl, *Surf. Interface Anal.*, 2016, **48**, 261–273.

57 R. A. Evarestov, A. Platonenko, D. Gryaznov, Y. F. Zhukovskii and E. A. Kotomin, *Phys. Chem. Chem. Phys.*, 2017, **19**, 25245–25251.

58 A. de Jamblinne de Meux, G. Pourtois, J. Genoe and P. Heremans, *J. Appl. Phys.*, 2018, **123**, 161513.

59 R. Thapa, S. Ghosh, S. Sinthika, E. Mathan Kumar and N. Park, *J. Alloys Comp.*, 2015, **620**, 156–163.

60 D. Bridget Williams, W. Kaminsky, J. M. Mayer and K. I. Goldberg, *Chem. Commun.*, 2008, 4195.

61 M. G. Crestani, A. Steffen, A. M. Kenwright, A. S. Batsanov, J. A. K. Howard and T. B. Marder, *Organometallics*, 2009, **28**, 2904–2914.

62 H. Baumgarth, T. Braun, B. Braun, R. Laubenstein and R. Herrmann, *Eur. J. Inorg. Chem.*, 2015, **2015**, 3157–3168.

63 A. Escobedo-Morales, R. Esparza, A. García-Ruiz, A. Aguilar, E. Rubio-Rosas and R. Pérez, *J. Cryst. Growth*, 2011, **316**, 37–41.

64 N. Uekawa, N. Mochizuki, J. Kajiwara, F. Mori, Y. J. Wu and K. Kakegawa, *Phys. Chem. Chem. Phys.*, 2003, **5**, 929–934.

65 M. Sun, W. Hao, C. Wang and T. Wang, *Chem. Phys. Lett.*, 2007, **443**, 342–346.

66 G. L. Gutsev, B. K. Rao and P. Jena, *J. Phys. Chem. A*, 2000, **104**, 11961–11971.

67 M. N. Amini, H. Dixit, R. Saniz, D. Lamoen and B. Partoens, *Phys. Chem. Chem. Phys.*, 2014, **16**, 2588.

68 M. Dekkers, G. Rijnders and D. H. A. Blank, *Appl. Phys. Lett.*, 2007, **90**, 021903.

69 Y. Liu, H. Masumoto and T. Goto, *Mater. Trans.*, 2004, **45**, 3023–3027.

70 W. D. Ryden, A. W. Lawson and C. C. Sartain, *Phys. Rev. B*, 1970, **1**, 1494–1500.

71 S. G. Bhat, A. M. Koshy, S. Pittala and P. S. A. Kumar, AIP Conf. Proc., 2017, **1859**, 020007.